

## Article

# Observational Analysis of a Wind Gust Event during the Merging of a Bow Echo and Mini-Supercell in Southeastern China

Hui Zheng <sup>1,2,3</sup>, Yuchun Zhao <sup>2,3,\*</sup> , Yipeng Huang <sup>3</sup> , Wei Zhang <sup>3</sup>, Changrong Luo <sup>3</sup>, Ming Wei <sup>4</sup> and Xinfu Qiu <sup>5</sup>

<sup>1</sup> School of Applied Meteorology, Nanjing University of Information Science and Technology, Nanjing 210044, China; 20161112069@nuist.edu.cn

<sup>2</sup> State Key Laboratory of Numerical Modeling for Atmospheric Science and Geophysical Fluid Dynamics (LASG), Institute of Atmospheric Physics, Chinese Academy of Sciences, Beijing 100029, China

<sup>3</sup> Xiamen Key Laboratory of Straits Meteorology, Xiamen Meteorological Bureau, Xiamen 361013, China; harrisonyp@163.com (Y.H.); zw880810@126.com (W.Z.); luo323@sina.com (C.L.)

<sup>4</sup> Collaborative Innovation Center for Forecast and Evaluation of Meteorological Disasters, Nanjing University of Information Science and Technology, Nanjing 210044, China; mingwei@nuist.edu.cn

<sup>5</sup> School of Geographic Sciences, Nanjing University of Information Science and Technology, Nanjing 210044, China; xfqiu135@nuist.edu.cn

\* Correspondence: zhaoych@cma.gov.cn

**Abstract:** The merging of a fast-moving bow echo with a convective cell of a hook-echo signature was studied by using polarimetric radar detections. Gusts with wind speeds near  $35 \text{ m s}^{-1}$  were recorded by the surface station, which caused significant damage. A convective cell with a mesovortex signature, which is hereafter referred to as a mini-supercell, was observed over the northeast of the bow echo before the convective merging. It was found that the mesovortex possessed cyclonic circulation and resembled a supercell-like feature. The merging of the bow echo and the mini-supercell strengthened the updraft near the apex of the bow echo. The enhanced updraft was also demonstrated by the appearance of a differential reflectivity ( $Z_{DR}$ ) column with a topmost height of 4 km above the melting layer ( $\sim 4 \text{ km}$ ). The bow was separated into northern and southern sectors after merging with the mini-supercell, leading to the gusty wind over the surface of the south sector.

**Keywords:** convective merging; wind gust; bow echo; mini-supercell; dual-polarization radar



**Citation:** Zheng, H.; Zhao, Y.; Huang, Y.; Zhang, W.; Luo, C.; Wei, M.; Qiu, X. Observational Analysis of a Wind Gust Event during the Merging of a Bow Echo and Mini-Supercell in Southeastern China. *Atmosphere* **2021**, *12*, 1511. <https://doi.org/10.3390/atmos12111511>

Academic Editor: David K. Adams

Received: 14 September 2021

Accepted: 13 November 2021

Published: 16 November 2021

**Publisher's Note:** MDPI stays neutral with regard to jurisdictional claims in published maps and institutional affiliations.



**Copyright:** © 2021 by the authors. Licensee MDPI, Basel, Switzerland. This article is an open access article distributed under the terms and conditions of the Creative Commons Attribution (CC BY) license (<https://creativecommons.org/licenses/by/4.0/>).

## 1. Introduction

Convective merging is a common weather phenomenon. Researchers began to study the merging of convective systems as early as the 1940s [1] and conducted numerous observational studies later on [2–6]. Convective merging is a complex nonlinear process involving dynamics and cloud physics, and the newly formed systems are characterized by significantly increased cloud thicknesses and sizes, strengthened upward motions, and greater precipitation areas and intensities [7–12].

The merging of a bow echo and a convective cell is an uncommon process, which is caused by the difference in moving speed between two different types of convective systems [13]. Bow echoes usually develop from squall lines and can also be formed by merging, for example, the merging of organized convective cells [14] or squall lines merging with a preline convective cell [15–18]. Fujita [19] first illustrated the typical characteristics of a bow echo, i.e., an inflow jet region accompanied by downbursts at the rear of the bow echo. Later on, many studies improved the conceptual model of bow echoes through investigating radar observations and numerical simulation [20–26]. They noted that a rear-inflow notch (RIN) boundary appearing in a bow echo was closely linked to the location of a rear-inflow jet (RIJ) and that notable outflows occurred on the two sides of the RIJ. These findings suggested a pair of counter-rotating vortices located on both ends of the bow

echo, that is, the book-end vortices [27]. They usually enhance the strengths of mid-level RIJs [28,29].

Studies on the merging of bow echoes and convective cells have yielded mixed results. For example, the merging of a bow echo and a supercell has two potential results: The supercell weakens and becomes part of the bow echo, thereby strengthening the bow echo; or the rapid weakening of the bow echo strengthens the supercell and leads to the development of a comma-shaped severe precipitation cell [30,31]. In addition, the merging of a bow echo and a convective cell is highly likely to trigger tornadoes [32]. Convective merging is one of the main error sources in numerical model prediction results [33]. How to provide early warnings of the development and the evolution of a merged convective system is still a challenge in the nowcasting of severe weather [34].

Doppler radars have played a vital role in nowcasting severe weather events and monitoring the evolutionary characteristics of convective structures [35]. In addition, the usage of dual polarization data provides more information for severe weather analysis. The updraft of a severe convective system can be identified by the characteristics of differential reflectivity ( $Z_{DR}$ ) [36]. Liquid water and partially frozen hydrometeors can be lofted considerably above the environmental  $0\text{ }^{\circ}\text{C}$  level in the updrafts of convective storms owing to the thermal perturbation from latent heating within the updraft and to the non-instantaneous drop freezing [37]. In situ observations of the aircraft show  $Z_{DR}$  columns (upward extensions of positive  $Z_{DR}$ ) composed of substantial amounts of supercooled liquid water and collocated with the updraft [38–42]. The dual-Doppler analyses and numerical modeling results suggest that  $Z_{DR}$  columns collocate with updrafts and the depth of  $Z_{DR}$  columns tends to be proportional to the updraft intensity [43–45].

On 30 April 2019, a bow echo intercepted a supercell-like convective cluster (mini-supercell) occurring in Southeastern China and merged into a stronger convective system. This case is not the same as those studied previously [30–32]. This merging process did not produce a tornado, but a damaging straight-line wind. As a specific type of convective cell, a supercell is larger, longer-lived and more violent than an ordinary convective cell. In radar observation, the echo structure of a supercell has a vault (weak echo region, WER), an overhang echo, an echo wall in the vertical direction, and a hook echo in the horizontal direction [46]. The mini-supercell is a small, moderately intense supercell storm with characteristics similar to those of classic supercells, including a unicellular echo with multicellular substructures, an extended lifetime, a collar cloud, and a flanking line of cumulus [47]. The merging process of a bow echo and a mini-supercell led to a short period of heavy rainfall and an instantaneous wind gust with a speed exceeding  $34.3\text{ m s}^{-1}$ . A gusty wind of this intensity was not predicted in the nowcasting of the meteorological department. Although severe convective weather occurs frequently in Southeast China, the merging process of a bow echo and a convective cell is not common. In order to understand the causes of this damaging wind and provide a basis for the early warnings of similar merge processes in the future, this case needs to be studied. The gust front is related to a downburst, and the RIJ of the bow echo plays an important role in damage wind. In this study, we will focus on analyzing the evolutionary characteristics of an RIJ during the merging process and examine the possible formation mechanism for the intense gusty wind.

Section 2 describes the data and the methodology. Section 3 presents the synoptic background. Section 4 describes the merging process and the evolution of the RIJ. The possible formation mechanism for the gusty wind and the impacts of the merge upon the gusty wind formation are also examined. Section 5 provides a discussion. The conclusions are summarized in Section 6.

## 2. Data and Methods

### 2.1. Data

The locations of the instruments used in this study are summarized in Figure 1. The region within the black box is the main study area; that is, the location of the wind gust

event and its associated convective processes (Figure 1a). The observations from the China Meteorological Administration (CMA) operational S-band dual-polarization Doppler radar at Xiamen (WSR-98D; DPXM) in the study area were used to document the evolution of the merging process. The other two CMA operational S-band radars (WSR-88D; BFQZ, BFLO) located at Quanzhou and Longyan near the study area were also employed. All radars operated in VCP21 mode, which completed a volume scan with nine elevations ( $0.5^\circ$ ,  $1.5^\circ$ ,  $2.4^\circ$ ,  $3.4^\circ$ ,  $4.3^\circ$ ,  $6.0^\circ$ ,  $9.9^\circ$ ,  $14.6^\circ$ , and  $19.5^\circ$ ) every 6 min. The unambiguous range was 150 km, and the unambiguous velocity was  $26.5 \text{ m s}^{-1}$ . The range resolution of the radar was 0.5 km, and the beam width was  $1^\circ$ . The quality control procedures were performed on each elevation. Considering the topographical impacts of the low altitude in the study area, the Doppler velocities of  $0.5^\circ$  and  $1.5^\circ$  with values less than  $0.25 \text{ m s}^{-1}$  and the corresponding reflectivity data were excluded to reduce the contamination of nearby ground clutter and any remaining spurious information in the computation of the deviation of each data point from its local mean [48].

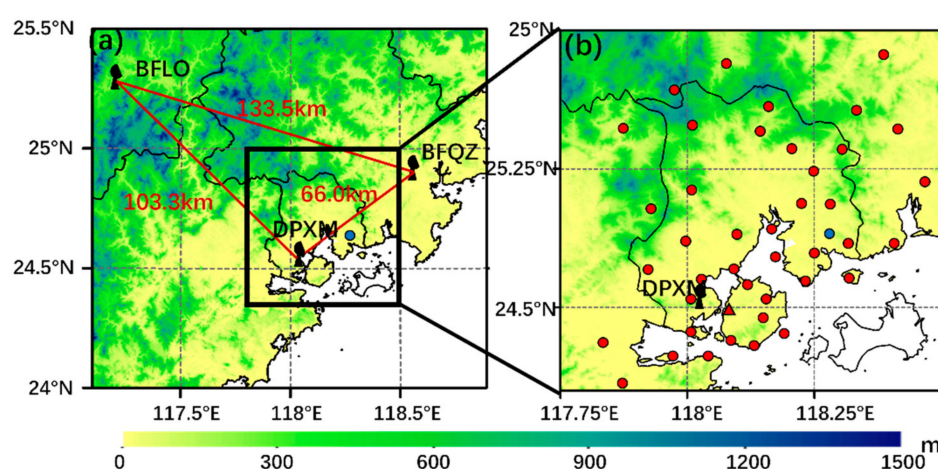


**Figure 1.** Multiple observations used in this study: (a) three operational S-band Doppler radars (DPXM, BFQZ, and BFLO); and (b) automatic weather stations (AWSs; indicated by red and blue dots) and a radiosonde (indicated by the red triangle). The blue dot in (a) indicates the site where the wind gust with a maximum speed of  $34.3 \text{ m s}^{-1}$  was recorded.

The automatic weather stations (AWSs) used in this study are shown by the red dots in Figure 1b (the area indicated by the black square in Figure 1a). The 5 min interval surface observation data around the wind damage site were used to describe the surface chart during the merging process. Radiosonde station data (indicated by the red triangle in Figure 1b) were used to analyze wind, temperature, and humidity profiles and to determine convective parameters. The six-hourly ( $1^\circ \times 1^\circ$ ) reanalysis data downloaded from the website of the U.S. National Centers for Environmental Prediction (NCEP) were used to describe the synoptic pattern. The local standard time (LST;  $\text{LST} = \text{UTC} + 8$ ) was used in this paper.

## 2.2. Processing of Radar Data

The  $Z_{DR}$  column was used to identify the updraft locations in severe thunderstorms [37]. A three-dimensional contiguous volume of  $Z_{DR}$  was identified and defined as a  $Z_{DR}$  column, when the  $Z_{DR}$  elements in the three-dimensional contiguous volume were all greater than 1 dB and extended up to an altitude at least 500 m higher than the environmental  $0^\circ \text{C}$  level and their corresponding reflectivity were all greater than 10 dBZ.

The technique of retrieving a wind field from dual-Doppler radar data, which is based on the ODD (Over-Determined Dual-Doppler) technique by Ray et al. [49], was developed by Luo et al. [50]. This technique makes it possible to realize the advantages of a radar network and obtain optimum wind fields among those retrieved from each pair of multiple

radar systems. The retrieved wind was used to analyze the evolution of the mesoscale wind structure during the merging. The details of this method are provided in Appendix A.

### 3. Synoptic Pattern and Convective Environment Overview

#### 3.1. Synoptic Pattern

Figure 2 shows the synoptic chart at 14:00 LST on 30 April 2019. The 200 hPa divergence region relating to South Asia high over the Indochinese Peninsula, which was conducive to convective development, was over Southeastern China (Figure 2a). The 500 hPa subtropical high was located to the south of the study area. The geopotential height in the study area was approximately 5820 geopotential meters (Figure 2b). A southerly trough was located over Southwestern China that was relatively weak in intensity. The region where the merge process occurred was under the control of a southwesterly flow in front of the southerly trough. The shear lines on 850 hPa (Figure 2c) and 925 hPa (Figure 2d) were located over this region, extending inland towards South China and gradually moving southward. There was a notable low-level southwesterly jet on the south side of the shear line on 925 hPa (Figure 2d), with its center located over the coastal region of South China and its intensity exceeding  $18 \text{ m s}^{-1}$ . A banded high pseudo-equivalent potential temperature ( $\theta_{se}$ ) tongue with a central value of 344 K extended from the coastal region of South China to the southern coastal region of Southeastern China.

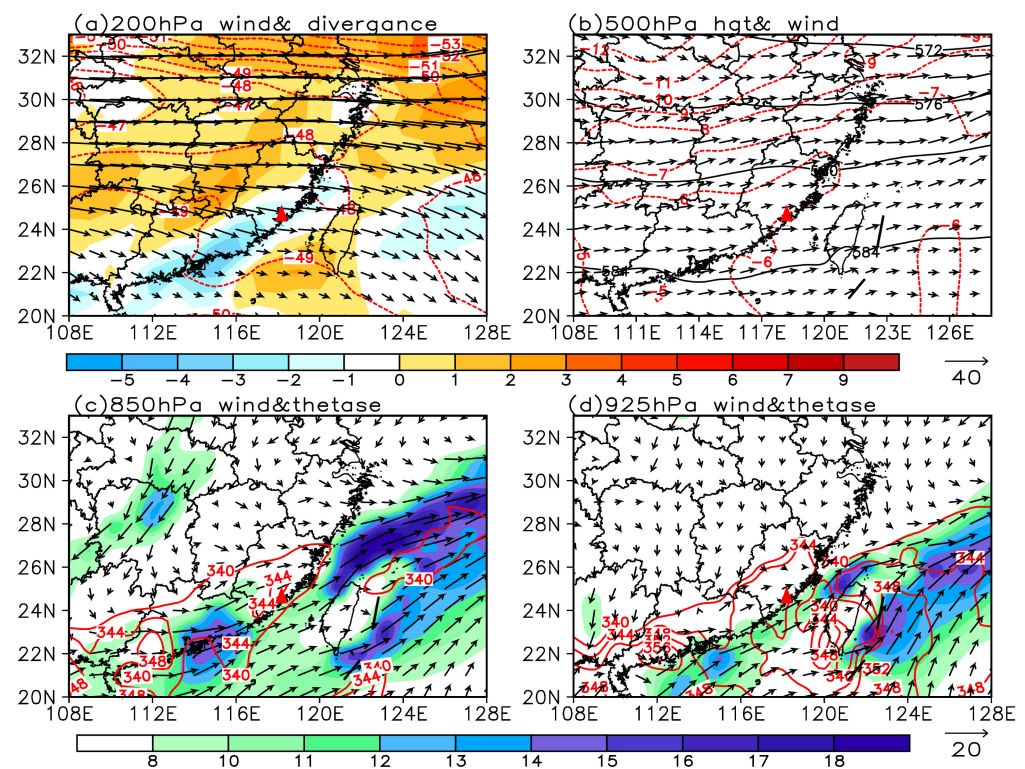


**Figure 2.** Weather charts at 14:00 LST on 30 April 2019: (a) 200 hPa wind (arrow), temperature (red broken lines; unit:  $^{\circ}\text{C}$ ), and divergence (shading; unit:  $10^{-5} \text{ s}^{-1}$ ); (b) 500 hPa geopotential height (isoline; unit: 10 geopotential meters), temperature (red broken lines; unit:  $^{\circ}\text{C}$ ), and wind (arrow; unit:  $\text{m s}^{-1}$ ); (c) 850 hPa; and (d) 925 hPa winds (arrow; unit:  $\text{m s}^{-1}$ ) with a total wind speed (shading; unit:  $\text{m s}^{-1}$ ) and  $\theta_{se}$  (contour; unit: K). The red triangle marks the area where the wind gust occurred.

The analysis above indicated that there was a jet stream with high  $\theta_{se}$  over the coastal region of South China at 850 and 925 hPa. Thus, the coastal region was in a zone of high temperature and moisture, which implied greater instability, conducive to the triggering and maintenance of a convection.

### 3.2. Convective Environment

Figure 3a shows the skew T-log P diagram of the radiosonde station in Xiamen at 08:00 LST on 30 April 2019. The wind profile distribution indicated that the winds were uniformly southwesterly from the surface to 500 hPa. This was conducive to the transport of water vapor. The winds at the upper levels veered westerly strongly. The wind velocity at 300 hPa reached  $32 \text{ m s}^{-1}$ . The upper- and low-level vertical wind shears were significant, which could tilt the storm and reduce the obstruction of raindrops falling to the updraft so as to benefit the development of the convection. The vertical distribution of water vapor showed that a moist layer was located between 800 and 550 hPa. Dew point depression increased above the moist layer, indicating a dry layer above the middle troposphere. Another dry layer was below 800 hPa. This unique structure helped to increase conditional instability. The  $0^\circ \text{C}$  level was approximately 4.3 km above the ground. The K index was 36, the Showalter index was 0.45, and the convective available potential energy (CAPE) was  $619 \text{ J kg}^{-1}$ , while it reached  $1812 \text{ J kg}^{-1}$  12 h later. Thermodynamic instability can trigger the occurrence and development of severe convection and eventually result in severe convective weather events (e.g., lightning, strong winds, and short-term heavy rainfall). Figure 3b shows the profiles of potential temperature ( $\theta$ ),  $\theta_{se}$ , and saturated  $\theta_{se}$  [51]. The multilevel equivalent potential temperature declined with height in the mid–lower levels (850–600 hPa), where there existed obvious convective instability. In addition, the low-level warm advection helped to increase the vertical instability.

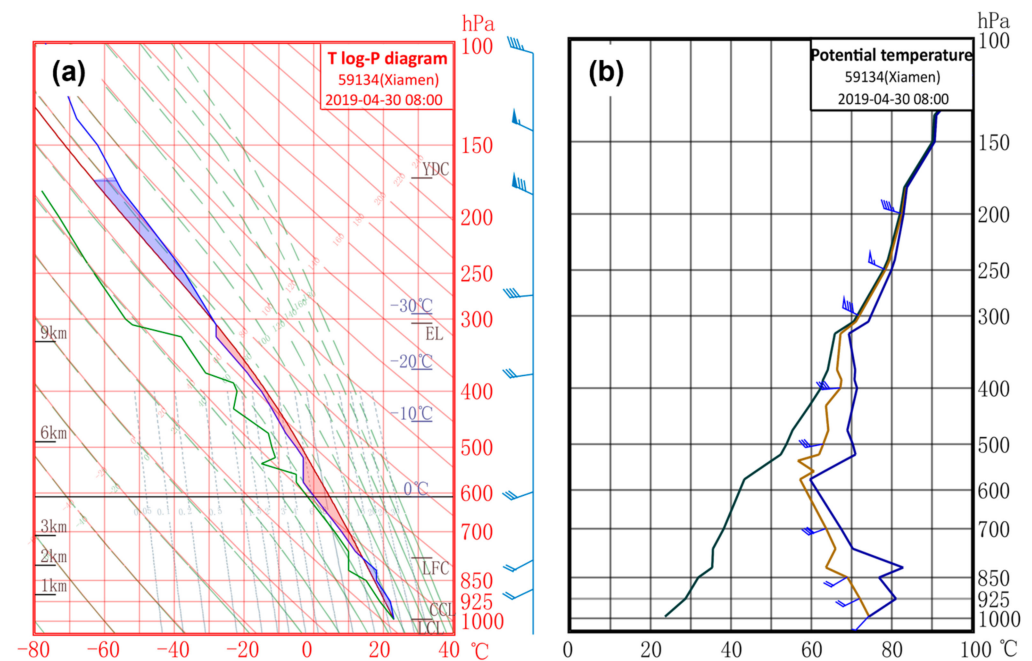


**Figure 3.** (a) Skew T-log P diagram of the sounding at 08:00 local standard time (LST) on 30 April 2019 with temperature (in blue), dew point temperature (in green), and stratification (in red) curves. Wind bars (long feather:  $4 \text{ m s}^{-1}$ ) are plotted on the right. Heights are given along the standard pressure levels (meters above ground level, or m AGL). The  $0^\circ \text{C}$  level was at  $\sim 4.3$  km AGL. (b) Potential temperature (in black),  $\theta_{se}$  (in brown), and saturated  $\theta_{se}$  (in blue).

## 4. Observational Features of Convective Merging Processes

### 4.1. Overview on Merging Processes

A linear convective system moved northeastward along the coastline in South China on the afternoon of 30 April 2019. The southern side of the linear echo evolved into a bow echo (Figure 4a) and moved at a higher speed of  $17 \text{ m s}^{-1}$  at 16:30 LST. In the regions impacted by the linear convective system, the gust wind speed was observed to be greater than  $18 \text{ m s}^{-1}$  on the south side of the linear convective system, that is, the location of the

bow echo. Between 17:30 and 18:00 LST, the bow echo encountered and merged with an isolated supercell-like cell (mini-supercell; Figure 4b). A wind gust event occurred near the merging region. The maximum wind gust observed at the AWS (F2293 Dazhai) in Xiamen reached  $34.3 \text{ m s}^{-1}$ . The wind direction turned from southeasterly to northwesterly and the surface pressure rose to 1.9 hPa within 10 min, while the wind gust occurred (Figure 4c). Subsequently, the air temperature and the dew point temperature decreased quickly and significantly, and the air temperature decreased by  $3.7 \text{ }^\circ\text{C}$ , accompanied by a short-lived but severe precipitation of more than 1 mm per minute.

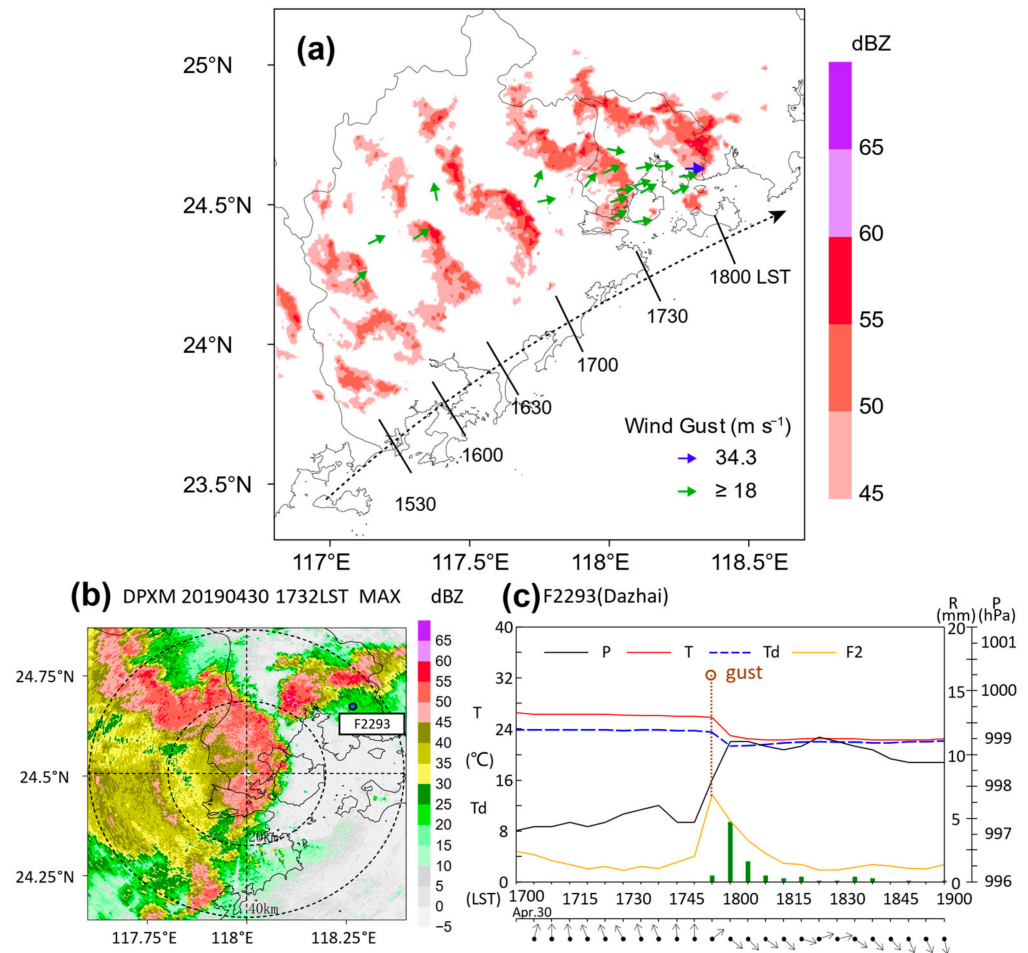


**Figure 4.** (a) The evolution of the bow echo (radar composite reflectivity factor  $\geq 45 \text{ dBZ}$ ) at 30 min intervals between 15:30 and 18:00 LST on 30 April 2019. The wind vector represents gusts ( $\geq 18 \text{ m s}^{-1}$ ) with different colors. (b) Locations of the bow echo and convective cells before merging (shaded, composite reflectivity; unit: dBZ). (c) Time series of the two-minute mean wind speed (yellow line; unit:  $\text{m s}^{-1}$ ) and direction (black arrow), the temperature (red line; unit:  $^\circ\text{C}$ ), the dew point temperature (blue dashed line; unit:  $^\circ\text{C}$ ), pressure (black line; unit:  $^\circ\text{C}$ ), and 5 min rainfall (green bars; unit: mm) from AWS F2293 (Dazhai). The peak gust is shown by the brown open circle.

## 4.2. Development and Evolution of the Mini-Supercell

### 4.2.1. Development of the Mini-Supercell

At 14:00 LST on 30 April 2019, the average surface air temperature in Xiamen was approximately  $30 \text{ }^\circ\text{C}$  (Figure 5a), and southerly wind prevailed in this region. Beginning at 15:00 LST, there was ephemeral rain in the mountainous area in the north of Xiamen (not shown), which led to a notable decrease of  $2\text{--}6 \text{ }^\circ\text{C}$  in surface air temperature (Figure 5b). In the precipitation area, the surface wind direction turned to the north, accompanied by an increase in relative humidity and a small increase in surface pressure. These characteristics

were consistent with the outflow boundary at the leading edge of a cold pool, which might result from precipitation and evaporation [52]. A front-like interface formed in the front of the cold pool. Due to the notable changes in wind speed and direction, an intense convergence of air flow appeared along the interface. As demonstrated in Figure 5c, the surface wind field in Central Xiamen presented a pronounced convergence following the precipitation in the north. In addition, convective cells appeared in the surface convergence zone and developed rapidly. The convective cells were organized and developed along the surface convergence zone before, merging, developing (Figure 5d) moving slowly to the northeast, and finally merged with the bow echo.

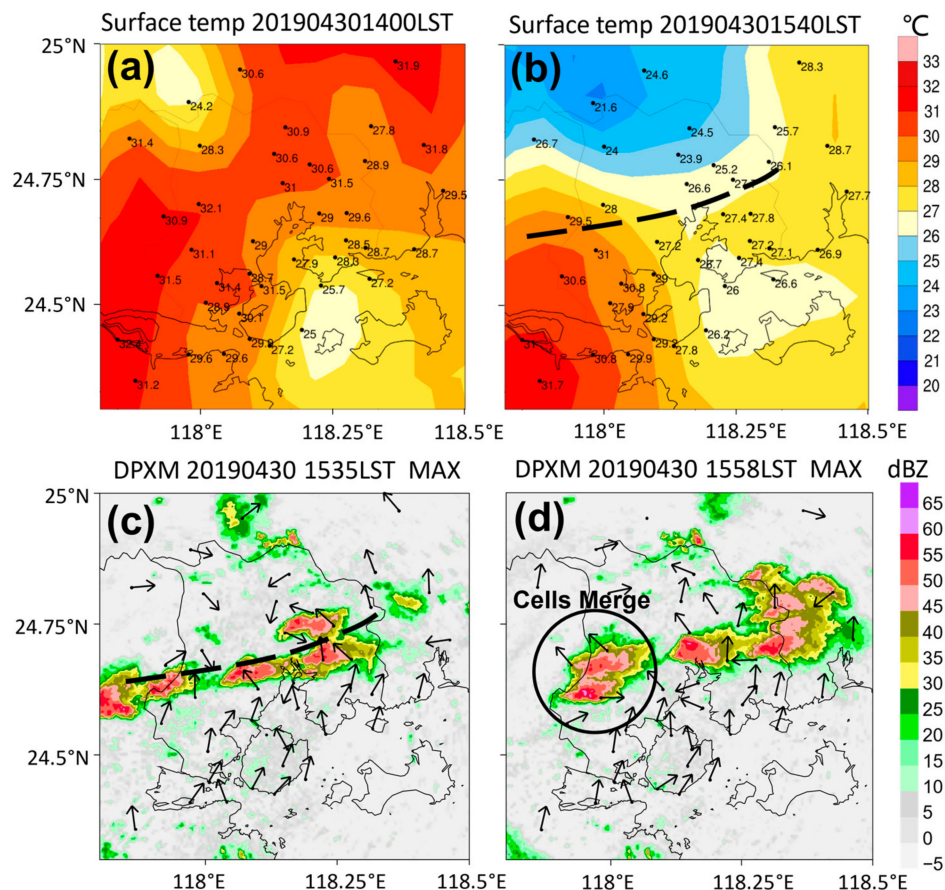


**Figure 5.** The surface temperatures (shaded; unit: °C) at 14:00 LST (a) and 15:40 LST (b) and the surface wind field (arrow, units:  $\text{m s}^{-1}$ ) and the radar composite reflectivity (shaded, units: dBZ) at 15:35 LST (c) and 15:58 LST (d) on 30 April 2019. The dashed line in (b,c) indicates the surface convergence line.

Before merging with the bow echo, the local convection developed into three severe convective cells, i.e., A (a mini-supercell with a hook-shaped echo), B, and C (Figure 6a). The merging process mainly occurred between mini-supercell A and the bow echo, while cells B and C gradually weakened. The size and the intensity of the mini-supercell were weaker than those of a typical supercell, but they have similar structural characteristics. The vertical structure of the mini-supercell is shown in sections D–E in Figure 6a, parallel to the storm's path (Figure 6c), and sections F–G in Figure 6a, perpendicular to the storm's path (Figure 6d). There were a bounded weak echo region (BWER), an overhang echo, and an echo wall. The BWER usually occurs, when water droplets are carried and lifted up by a strong updraft. The occurrence of a BWER generally indicates that the updraft rotates significantly around the vertical axis of the convective cell. This rotation has been verified by Doppler velocity data. The plan position indicator (PPI) of the mini-supercell indicated

a Doppler velocity dipole located at 4–5 km, with a maximum radial velocity difference of  $29.5 \text{ m s}^{-1}$  (Figure 6b).

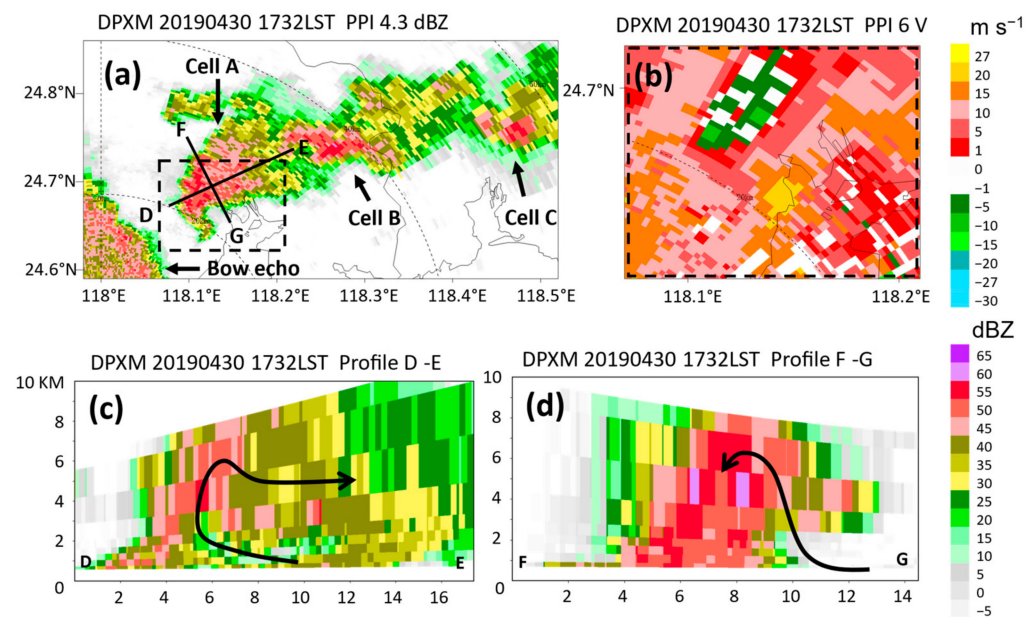


**Figure 6.** (a) Mini-supercell with a hook-shaped structure (shaded,  $4.3^\circ$  plan position indicator (PPI); unit: dBZ). (b) Mini-supercell with a velocity dipole (shaded,  $6^\circ$  PPI, and the direction of the positive Doppler radial velocity is northeast; unit:  $\text{m s}^{-1}$ ) in PPI before merging with the bow echo. (c) Cross-section (shaded; unit: dBZ) along sections D–E in (a). (d) Transverse section (shaded; unit: dBZ) along sections F–G in (a).

#### 4.2.2. Variation Features in the Mini-Supercell

A dual-polarization radar was used to track the strong echo centers of the mini-supercell at the time when the merging began to take place. The cross-section along the strong center was interpolated at the same intervals, as the radar volume scanned. The radar reflectivity ( $Z$ ) at 17:40 LST (Figure 7c) showed that the 50 dBZ echoes reached a height of 7 km before the merging, and that the vertical height of the  $Z_{DR}$  column was only approximately 6.5 km (the height of the  $0^\circ\text{C}$  layer was 4.3 km). Five minutes later (at 17:45 LST), there was an obvious echo connection between the two convective systems (Figure 7d). The mini-supercell connected with the bow echo, exhibiting a feature of the BWER. At that time, the vertical height of the  $Z_{DR}$  column increased to approximately 8 km. The rising of the  $Z_{DR}$  column suggested that the vertical motion began to intensify. The negative Doppler velocity ( $V$ ) portion of the region, where the mini-supercell was located, decreased markedly in size. The wind velocity at a height of 5–7 km increased. The front of the positive velocity region relating to the bow echo exhibited a feature of convergent uplifting. At 17:50 LST (Figure 7e), the  $Z_{DR}$  column continued to rise up, and its maximum height reached approximately 8.5 km. The strong echo center and the echo bottom were both lifted upward. The characteristics of the BWER were prominent. The outflow region in the front of the bow echo was lifted upward. The upper-level strong velocity center relating to the mini-supercell further increased in size. The outflow region and the strong velocity center showed a tendency to join together. After only one volume scan (i.e., at 17:55 LST), the strong echo center reached a height of 9–10 km and exceeded 60 dBZ in intensity, and the 50 dBZ echoes reached a height of more than 11 km (Figure 7f). However, the main part of the  $Z_{DR}$  column lowered by 2.5 km, implying that the updraft began to weaken. At that time, the mini-supercell achieved its strongest state. The bottom of the echo lowered notably, indicating the occurrence of heavy precipitation. In addition, the outflow region of the bow echo connected with the Doppler velocity center of the mini-supercell. The strong

velocity center of the mini-supercell lowered significantly (a wind gust with a maximum of  $34.3 \text{ m s}^{-1}$  was observed at that time) (Figure 7b). Between 18:00 and 1805 LST (Figure 7g,h), there was subsequently a significant decrease in echo intensity. The echo lowered notably. The upper-level Doppler velocity center disappeared. The front of the low-level jet relating to the bow echo descended toward the ground.

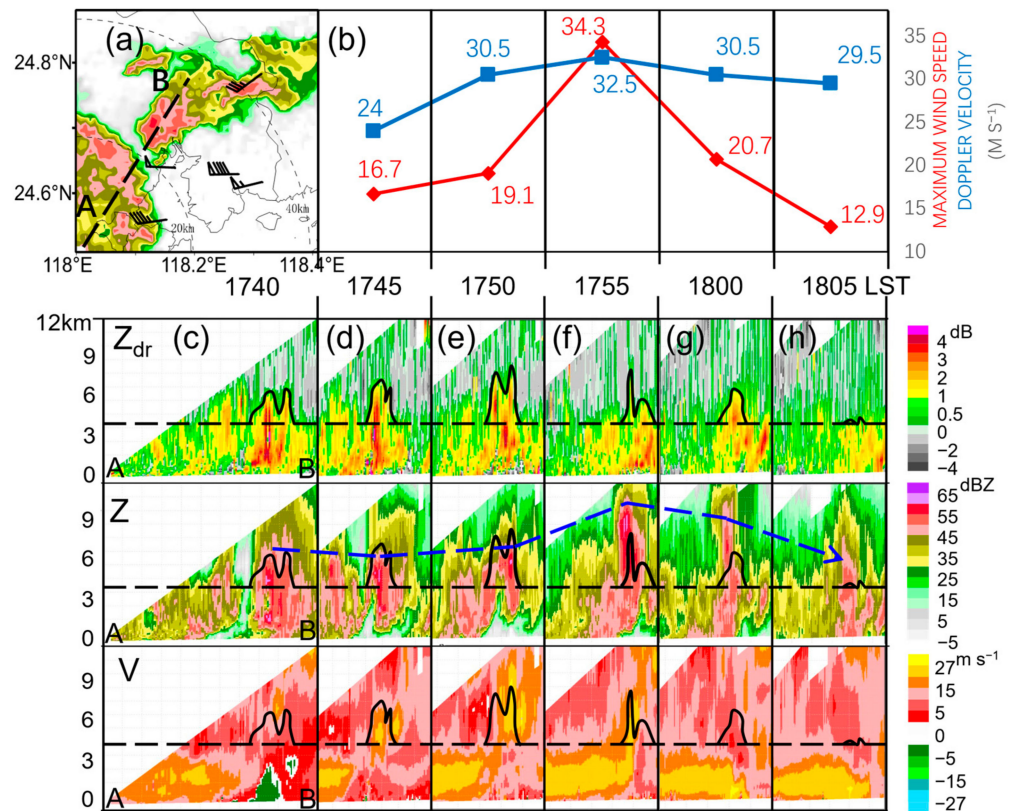


**Figure 7.** (a) The  $1.5^\circ$  PPI radar reflectivity distribution of the mini-supercell and the bow echo, the wind barbs (the magnitudes of the short barb, the long barb, and the flag are 2, 4, and  $20 \text{ m s}^{-1}$ ) mark the locations of the maximum wind speed observed every 5 min (17:45 LST to 18:05 LST from left to right). (b) The observed extreme gust wind speed nearby (red line; unit:  $\text{m s}^{-1}$ ) and the maximum horizontal distribution of the Doppler velocity (blue line; unit:  $\text{m s}^{-1}$ ). (c–h) The vertical structure evolutions of differential reflectivity ( $Z_{DR}$ ; shaded; unit: dB) (upper panels),  $Z$  (shaded; unit: dBZ) (middle panels), and  $V$  (shaded, the mean Doppler velocity and the direction from A to B is positive (southwesterly); unit:  $\text{m s}^{-1}$ ) (bottom panels) from 17:40 LST to 18:05 LST. The cross-sections in (c–h) are along lines A–B in Figure 7a. In Figure 7c–h, the black dashed line marks the  $0^\circ \text{C}$  level, the top of the  $Z$  of  $\geq 50 \text{ dBZ}$  is shown by a blue dashed line, and the vertical leading edge of  $Z_{DR}$  of  $\geq 1 \text{ dB}$  is shown by a black curve.

The evolution characteristics of the  $Z_{DR}$  column were indicative of the variation in updraft intensity. The merging strengthened the updraft and lifted the echo as a whole, increasing its intensity. However, the updraft was short-lived, and the height of the strong echo could not be maintained. The falling and dragging of precipitation particles contributed to the cold pool wind gust intensity.

#### 4.3. Evolution of the RIJ during the Merging

##### 4.3.1. Features of the Bow Echo before the Merging

The characteristics of the bow echo were typical before the merging. The PPI (Figure 8a) and the vertical cross-section (Figure 8c) of the reflectivity showed that a large gradient region was in the front of the bow echo, with a weak echo region (WER) on one side of the

inflow. The echo apex lied above the WER accompanying an RIJ boundary (i.e., an RIJ). The PPI of the Doppler velocity from the BFQZ showed that the negative velocity region of the jet protruded toward the front of the bow echo and that the front of the surface outflows was collocated with the apex location of the bow echo. The storm-relative velocity illustrated the book-end vortices characteristic of the bow echo clearly (the environmental average velocity of about  $20 \text{ m s}^{-1}$  of the bow echo area within the dashed line in Figure 8b was subtracted). The maximum velocity difference between the positive and negative centers reached  $26 \text{ m s}^{-1}$ . The cross-section along lines A–B (the direction in which the cell was moving) (Figure 8d) showed that the core of the RIJ was at a height of 3 km and the jet ( $\geq 20 \text{ m s}^{-1}$ ) reached an altitude of 4–5 km. The front of the high velocity in the lower layer was in a high reflectivity gradient region and also in the front of the bow echo. The moving direction of the convective system implied that the soon-to-be-merged region was located at the apex of the bow echo, rather than in its book-end vortices region.

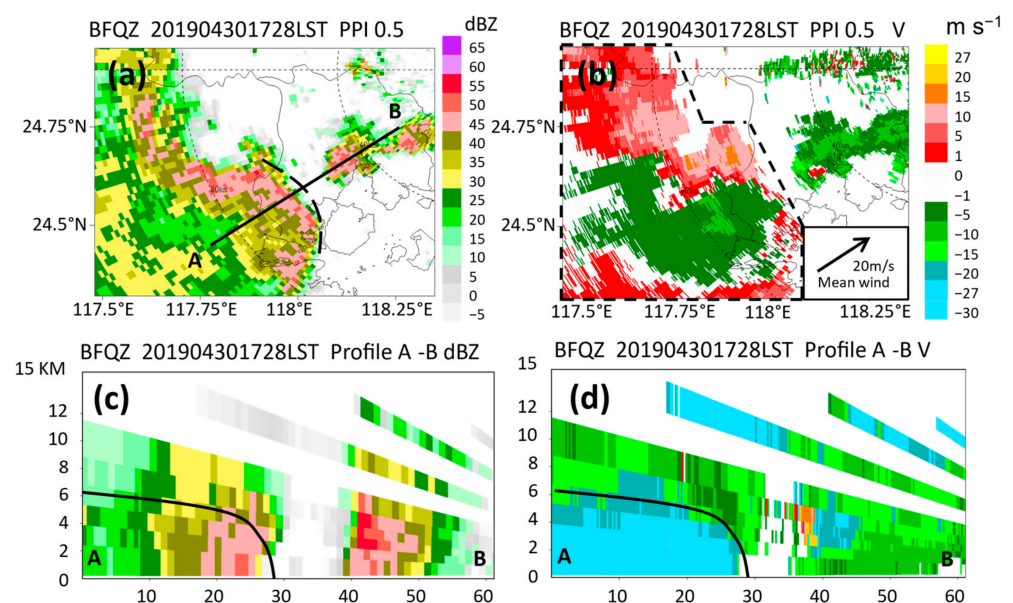


**Figure 8.** (a) Reflectivity (shaded; unit: dBZ) of BFQZ at  $0.5^\circ$  PPI at 17:28 LST. Doppler velocity (shaded; unit:  $\text{m s}^{-1}$ ; dashed area; storm-relative velocity; the storm motion is shown in the bottom-right panel) (b) and their corresponding cross-sections of (c) reflectivity (shaded; unit: dBZ) and velocity (shaded; unit:  $\text{m s}^{-1}$ ) (d) along black lines A and B in (a).

#### 4.3.2. Evolution of the RIJ during the Merging

The bow echo was split into two parts during the merging. Then, the bow echo encountered the mini-supercell at about 17:33 LST (Figure 9a). When the bow echo intercepted the mini-supercell at 17:39 LST (Figure 9b), the frontal boundary of the negative Doppler velocity turned from a forward protruding shape to a smooth one. The reflectivity greater than 45 dBZ of the mini-supercell merged with the bow echo between 17:44 and 17:49 LST (Figure 9c,d), and the velocity boundary shape of the bow echo changed significantly. The merging occurred near the apex of the bow echo. The  $1.5^\circ$  Doppler velocity showed that the RIJ extended to the two flanks of the merging area. The wind gust was collocated with the extended region of the RIJ in the south. In addition, the velocity evolution indicated that the negative dipoles of the mini-supercell merged with the south part of the velocity boundary (Figure 9d,e), with the positive dipole disappearing at 17:59 LST.

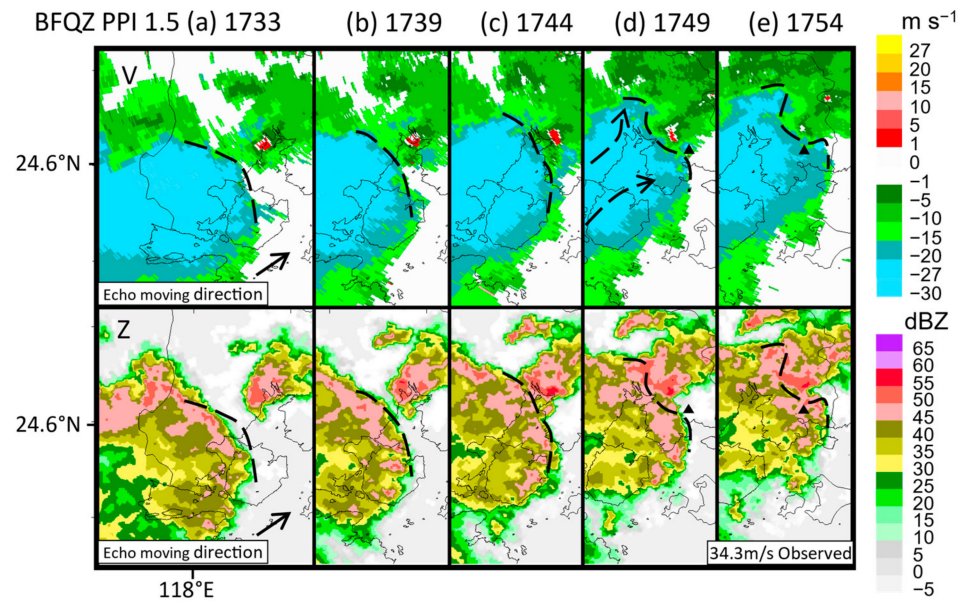


**Figure 9.** Doppler velocities (upper panels) (shaded; unit:  $\text{m s}^{-1}$ ) and reflectivity (bottom panels) (shaded; unit: dBZ) at  $0.5^\circ$  PPI observed by BEQZ at 17:33 LST (a), 17:39 LST (b), 17:44 LST (c), 17:49 LST (d), and 17:54 LST (e). The dashed line indicates a front of radial velocity greater than  $20 \text{ m s}^{-1}$  relating to the bow echo. The dashed arrows show the inflows. The black triangles indicate the locations of wind damage.

The low-level cyclonic-circulation structure of the mini-supercell was destroyed during the merging at 17:50–17:55 LST, but the middle-level cyclonic-circulation structure still existed, overlapping with the RIJ of the bow echo in the vertical direction. The multiple PPIs of DPXM indicated that five minutes before the occurrence of the wind gust, the reflectivity values in the merging core region close to the mini-supercell were greater than 60 dBZ and located 6.5 km above the ground (i.e., at 17:50 LST) (Figure 10a; “SC” means mini-supercell, and “RIN” refers to rear-inflow notch which indicated the position of the RIJ). The Doppler velocities showed that a significant Doppler velocity dipole implying a typical cyclonic structure existed near the strong echo center. In the southern sector of the extended region of the bow echo (also the extended area of the RIJ), a Doppler velocity ambiguity appeared at the core of the jet (Figure 10c). At 17:55 LST, the high reflectivity core remained above 6.5 km with the movement of the bow echo. The strong echo center was almost kept quasi-stationary, and the dipole size in the middle layer decreased. The RIJ of the southern part of the bow echo extended below the mesocyclone, overlapping with a positive vorticity region. The intensity of the RIJ was strengthened.

#### 4.4. Kinematic Features during the Merging

The retrieved wind field showed that the RIJ separated and subsided during the bow echo merging with the mini-supercell. At 17:45 LST (Figure 11a), a weak velocity region with an echo intensity of over 40 dBZ appeared in the joining area of the two systems, when the mini-supercell came into contact with the echo. The RIJ of the bow echo separated into two sectors. The south part of the RIJ extended toward the south side of the mini-supercell, becoming more prominent at 17:50 LST (Figure 11b). The RIJ separation might be a result of the precipitation impeding. During the merging, the RIJ extended to both sides of the weak velocity area (17:55 LST; Figure 11c). The reflectivity in the weak velocity area increased, and the RIJ in the south was significantly strengthened.

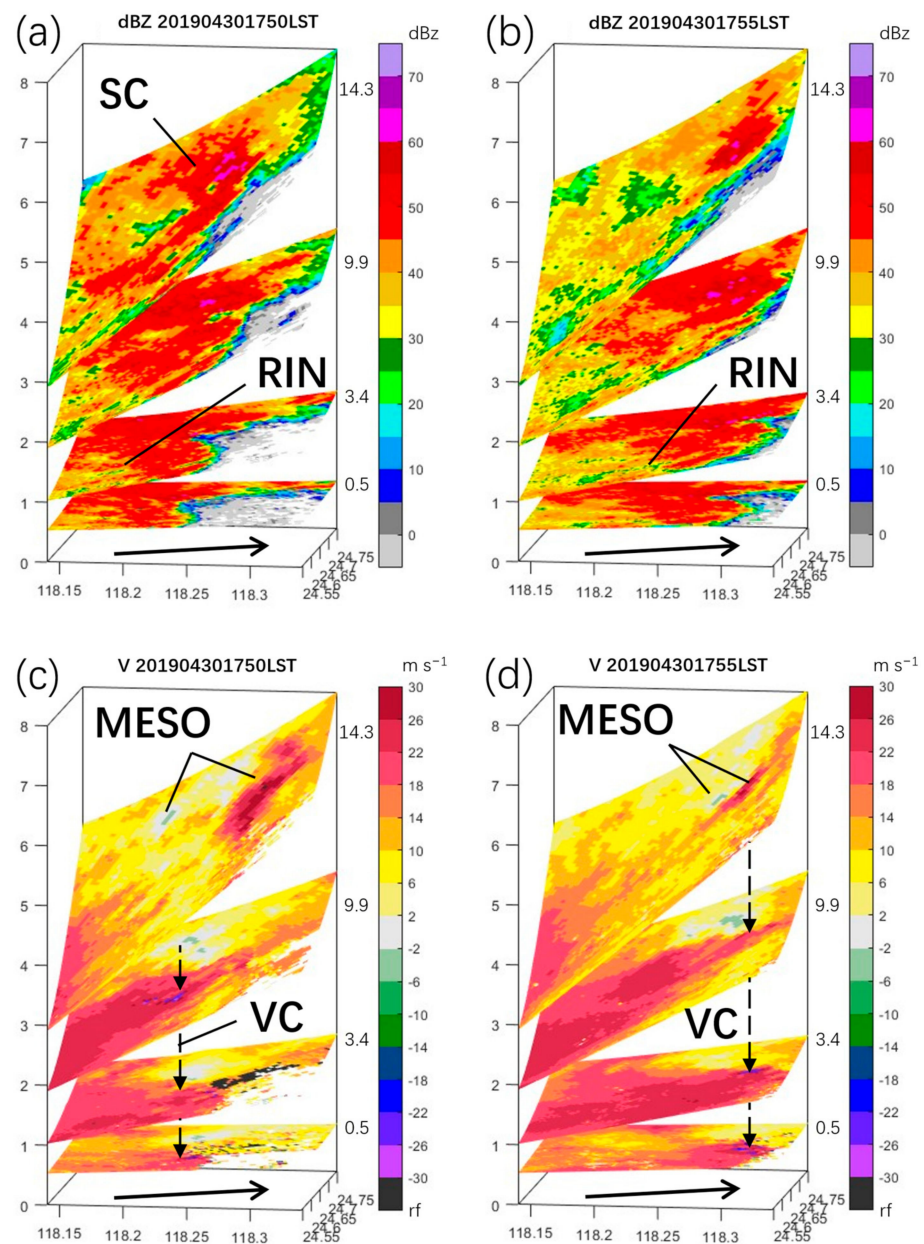


**Figure 10.** Reflectivity (shaded; unit: dBZ) structures of multiple PPIs (0.5°, 3.4°, 9.9°, and 14.3°) at 17:50 LST (a) and 17:55 LST (b). Doppler velocity (shaded; unit: m s<sup>-1</sup>) structures of multiple PPIs (0.5°, 3.4°, 9.9°, and 14.3°) at 17:50 LST (c) and 17:55 LST (d). The black arrow indicates the moving direction of the system. Here, “SC” means mini-supercell, “RIN” refers to rear-inflow notch, “MESO” refers to mesocyclone, and “VC” (indicated by the dotted arrow) indicates velocity core in low-elevation PPIs.

A vertical cross-section along the southern RIJ (also across the damaging gust wind site) illustrated a downdraft when the gust wind occurred (Figure 11a–c). At 17:45 LST (Figure 11d), the reflectivity greater than 50 dBZ reached a height of 4.5 km, but it dropped to 3.5 km at 17:50 LST (Figure 11e). The dropping of the reflectivity core implied that a downdraft might occur. This was verified by the retrieved wind field at 17:55 LST (Figure 11f). The jet extending to the surface might contribute to the surface damage winds.

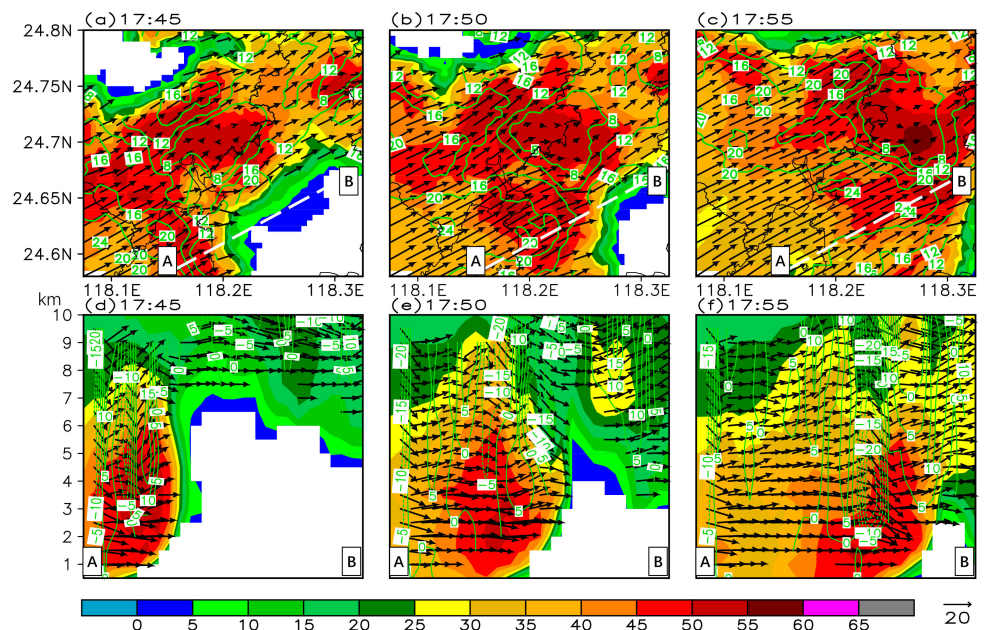


**Figure 11.** The retrieved horizontal wind field (black arrows; unit:  $\text{m s}^{-1}$ ), reflectivity (shaded; unit: dBZ), and absolute values of horizontal velocities (green contours; units,  $\text{m s}^{-1}$ ) at 3.5 km at 17:45 LST (a), 17:50 LST (b), and 17:55 LST (c). (d–f) The cross-sections of the retrieved wind field along lines A–B in (a) at the same times as in (a–c), respectively. The green contours in (d–f) mean the vertical component and the updraft were positive.

## 5. Discussion

In this study, the time variation when a bow echo and a mini-supercell merged was described in detail. The time variation of these observations can reveal the physical processes to a certain extent. This study helps to understand the possible mechanism of gusty winds in the merge process.

The cross-section evolution of the mini-supercell showed that the ZDR column was enhanced from the beginning of the merging process and reached 4 km above the  $0^\circ\text{C}$  level at 17:50 LST, which indicated that a severe updraft lifted water droplets to a maximum height of 4 km above the  $0^\circ\text{C}$  level before condensing into ice crystals. At the same time, the characteristics of the BWER in the vertical structure of reflectivity also indicated a severe updraft, which promoted the convective echo development. The updraft enhancement of the mini-supercell in the merging was probably caused by convergence associated with downburst outflow at the rear of the bow echo. Subsequently, the structure of the supercell was destroyed rapidly, and there was no updraft maintenance, resulting in the convective echo dropping and a stronger downdraft.

The fracture of the Doppler velocity front of the bow echo showed the blocking effect of the mini-supercell against the gust front during the merging process, which can be clearly seen in Figure 9. This phenomenon may occur because of the entrainment and dropping of liquid water particles in the mini-supercell, blocking the rapid movement of the bow echo. This terrain-like blocking effect divided the RIJ of the bow echo into two segments. The funneling effect formed by airflow obstruction may accelerate the jet flow on both sides of the mini-supercell in this process, and this feature was described in Section 4.4.

In conclusion, the formation of a ground gale may be due to the following reasons: (1) the downburst of the bow echo helped to produce the damaging straight-line winds. The maximum gust wind speed observed before merging was  $24.6 \text{ m s}^{-1}$ . Therefore, this is the basis for the formation of the intense gusty wind in the process; (2) in the merging process, the rapid enhancement of the updraft in the mini-supercell transported more precipitation particles to high altitudes and strengthened the subsequent subsidence. It

may add a downward component to the low-level jet and strengthen the gust wind on the ground; (3) the precipitation particles had a blocking effect on the jet flow. Specifically, the column blocking of precipitation particles made the jet unable to pass through the convective cells, forming a barrier similar to a terrain to squeeze the jet and accelerate the flow locally; (4) in addition, the fast-moving bow echo led to a short merging time with the mini-supercell. It destroyed the low-level structure of the mini-supercell and formed an around flow. At a certain time (Figure 10), the vortex in the middle layer of the cell still existed and overlapped with the jet on the south side of the lower level in the vertical direction. Whether this feature enhanced the jet at the lower level needs further investigation and clarification.

## 6. Conclusions

In this study, we investigated the merging of a bow echo and a mini-supercell over Xiamen in Southeast China using multisource observation data such as multiple weather radars. The conclusions are as follows: The low-level water vapor and convective instability provided favorable conditions for the occurrence and development of the convective systems, such as the multiple convective cells and the bow echo. The bow echo and the mini-supercell merged near the apex of the bow echo, with the mini-supercell becoming strengthened. The updraft of the mini-supercell was strengthened significantly, which was evidenced by the morphological evolution of the  $Z_{DR}$  column and the structural characteristics of the mini-supercell. However, this phenomenon lasted only for a short period. The velocity boundary of the bow echo was destroyed, when the merging took place. The RIJ was separated into two parts, which extended toward the south and north flanks of the mini-supercell, respectively. The region affected by the south part of the RIJ core was approximately consistent with the area where the damage wind event was observed on the ground.

The merging led to a severe convective weather event. While a severe weather alert was issued operationally, this merging was not captured by the operational numerical forecast model. It is possible to forecast the upstream bow echo moving in the threaten region and its related severe convective weather. It is nearly impossible, however, to predict the intensity of the wind gust resulting from the merging of two convective systems. The Doppler velocity and the wind field retrieved from dual-radar data revealed the evolutionary characteristics of the merging of the bow echo and the mini-supercell with mesocyclone. The morphological evolution of the  $Z_{DR}$  column indicated the variation characteristics of the updraft during the merging. The updraft lasted only for a short time. The mini-supercell echoes in the merging were lifted, strengthened and then lowered rapidly. These processes were closely related to the time, when the surface wind gust occurred. The disruption of the bow echo velocity boundary accelerated the southern outflow jet. The movement of the Doppler velocity core was directly linked to the surface wind gust. The possible mechanism of the gust wind formation was discussed in Section 5. The merging was much more complicated when compared with the individually developing mini-supercell or bow echo. The merging mechanism and the primary cause of the damaging wind gust need to be further investigated. Particular focus should be placed on analyzing the following: (1) whether or not there exists a terrain-like blocking and accelerating effect when a bow echo is obstructed by a mini-supercell and the airflow separation appears in the two flanks of the mini-supercell; (2) whether or not the overlapping of the upper-level mesocyclone and the surface outflow front relating to the bow echo is directly linked to the occurrence of the wind gust; and (3) whether or not the downward momentum caused by heavy precipitation during the merging can directly contribute to the wind gust occurrence and the explosive development of the mini-supercell.

**Author Contributions:** Conceptualization, H.Z., Y.Z. and Y.H.; methodology, H.Z., C.L. and M.W.; investigation, Y.H. and W.Z.; software, H.Z. and W.Z.; writing—original draft preparation, H.Z.; writing—review and editing, H.Z.; supervision, Y.Z., Y.H. and X.Q.; project administration, X.Q., Y.Z. and Y.H. All authors have read and agreed to the published version of the manuscript.

**Funding:** This study was supported by the National Key R&D Program of China (2019YFB2102003), the open program of LASG, Institute of Atmospheric Physics, Chinese Academy of Sciences (grant number: 20210625), the National Natural Science Foundation of China (grant number: 41905049), and Xiamen science and technology program (grant number: 3502Z20206079).

**Institutional Review Board Statement:** Not applicable.

**Informed Consent Statement:** Not applicable.

**Data Availability Statement:** Publicly available datasets were analyzed in this study. Reanalysis data can be found here: <https://rda.ucar.edu/> (accessed on 13 November 2021). Various observations data were provided by the China Meteorological Administration (CMA). The data are not publicly available due to privacy or ethical concerns.

**Conflicts of Interest:** The authors declare no conflict of interest.

## Appendix A

The method used in this study is the dual-radar wind field inversion method by Luo et al. [50].

The radar-data-processing method can be briefly described as follows. (1) The selection of the dynamic earth coordinate system: The coordinate origin is set at the center of the earth, the Z axis passes through the target point and points to the zenith, and the X and Y axes point to the east and north of the target point, respectively. The coordinate system is not fixed and changes with the change in the target point. (2) The interpolation of the radar data: The radar volume scan data are interpolated into the retrieved grid. The retrieved grid adopts the grid with equal longitude, latitude, and height. The horizontal resolution used in this study was  $0.01^\circ \times 0.01^\circ$ , and the vertical resolution was 0.5 km. During interpolation, the Cressman distance weight interpolation method is adopted in the horizontal direction to suppress clutter. Linear interpolation is adopted, because there are few scanning levels in the vertical direction. (3) The realization of retrieving the wind field from the radial velocity: The iterative equations of the wind field are firstly established. The first estimated value of vertical velocity is then calculated using the mass continuity equation after setting the initial values of u-wind and v-wind. The iterative method is used to calculate the three-dimensional wind field.

By setting the coordinates of the observation target as P (0, 0, z), the frequencies can be expressed as:

$$v_{r1} = \frac{(-x_{01})}{R_1}u + \frac{(-y_{01})}{R_1}v + \frac{(z - z_{01})}{R_1}(w - w_t), \quad (\text{A1})$$

$$v_{r2} = \frac{(-x_{02})}{R_2}u + \frac{(-y_{02})}{R_2}v + \frac{(z - z_{02})}{R_2}(w - w_t), \quad (\text{A2})$$

$$R_1 = \left[ (-x_{01})^2 + (-y_{01})^2 + (z - z_{01})^2 \right]^{\frac{1}{2}}, \quad (\text{A3})$$

$$R_2 = \left[ (-x_{02})^2 + (-y_{02})^2 + (z - z_{02})^2 \right]^{\frac{1}{2}}, \quad (\text{A4})$$

where  $(x_{01}, y_{01}, z_{01})$  and  $(x_{02}, y_{02}, z_{02})$  are the coordinate positions of the two Doppler radar antennas;  $v_{r1}$  and  $v_{r2}$  are the Doppler velocity of the two radars;  $R_1$  and  $R_2$  are the distances of the two radars to the P;  $w_t$  is the falling velocity of precipitation particles in static atmosphere.

The vertical velocity was calculated by the continuity equation:

$$\frac{\partial w}{\partial z} = - \left( \frac{\partial u}{\partial x} + \frac{\partial v}{\partial y} \right), \quad (\text{A5})$$

$$w(z = z_0) = 0, \quad (\text{A6})$$

where  $z_0$  represents the height of the lower grid point of the lowest effective interpolation point.

The error of the retrieved wind field is related to the direction, speed, and spatial position of the wind field (Figure A1a). The authors of [53] point out that the best wind speed can be retrieved when the real wind direction is located on the angular bisector of the radial angle between the two radars and the best wind direction can be retrieved when the real wind direction is perpendicular to this angular bisector. When the included angle ( $\alpha$ ; Figure A1a) of the radial velocities detected by two radars is close to  $90^\circ$ , the error is small, and the error is largest at  $180^\circ$  (near the baseline) [54]. The smaller the distance ( $d$ ; Figure A1a) between the target and the baseline, the greater the error. Therefore, the following methods were adopted for the radar networking of the retrieved wind field: (1) for areas covered by only one dataset, select this group; (2) for areas covered by two datasets, assess the included angle ( $\alpha$ ) between the retrieved point and the radar and select the group close to  $90^\circ$ . If the angle of the two groups in some areas is complementary, then assess the distance from the retrieved point to the radar baseline and select the group with the greater distance; (3) for the area covered by more than three groups of data, select the group of which the included angle between the retrieved point and the radar is closest to  $90^\circ$ .

In addition, due to the distance of radar BELO (103.3 km to DPXM and 133.5 km to BFQZ) and the high altitude (1.5 km), it was impossible to retrieve a wind field below 3 km with two other radars. The low-level wind field could not be retrieved near the baseline of DPXM and BFQZ (Figure A1b). The location of the mini-supercell was near the baseline, so it was necessary to define its updraft evolution features with the  $Z_{DR}$  column.

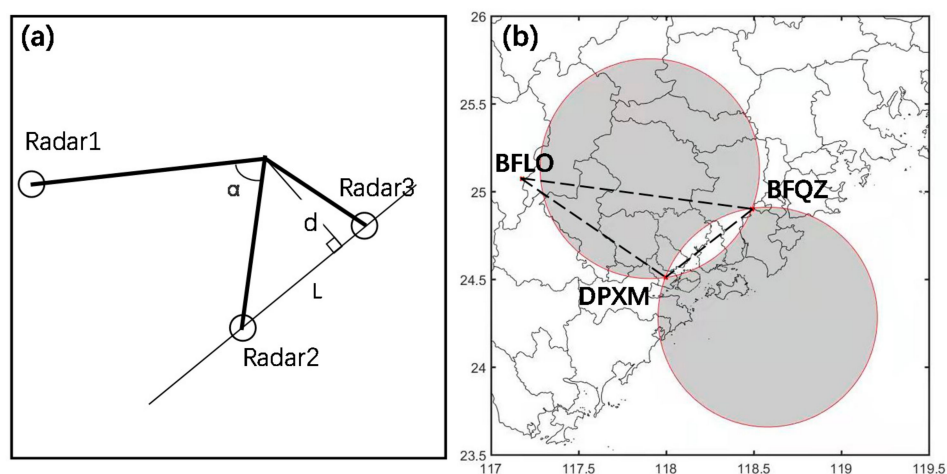


**Figure A1.** (a) Diagram of influencing factors for the dual-radar retrievals error. (b) The baseline of the three radars (black dashed line) and the optimal retrieved areas of DPXM and BFQZ (gray shadows).

## References

1. Byers, H.R.; Braham, R.R. *The Thunderstorm: Report of the Thunderstorm Project*; U.S. Government Printing Office: Washington, DC, USA, 1949; p. 287.
2. Malkus, J.S. SOME RESULTS OF A TRADE-CUMULUS CLOUD INVESTIGATION. *J. Meteorol.* **1954**, *11*, 220–237. [[CrossRef](#)]
3. Dennis, A.S.; Schock, C.A.; Koscielski, A. Characteristics of hail storms of western South Dakota. *J. Appl. Meteorol.* **1970**, *9*, 127–135. [[CrossRef](#)]
4. Browning, K.; Frankhauser, J.; Chalon, J.-P.; Eccles, P.; Strauch, R.; Merrem, F.; Musil, D.; May, E.; Sand, W. Structure of an Evolving Hailstorm Part V: Synthesis and implications for Hail Growth and Hail Suppression. *Mon. Weather Rev.* **1976**, *104*, 603–610. [[CrossRef](#)]
5. Lemon, L.R. The Flanking Line, a Severe Thunderstorm Intensification Source. *J. Atmos. Sci.* **1976**, *33*, 686–694. [[CrossRef](#)]
6. Barnes, S.L. Oklahoma Thunderstorms on 29–30 April 1970. Part II: Radar-Observed Merger of Twin Hook Echoes. *Mon. Weather Rev.* **1978**, *106*, 685–696. [[CrossRef](#)]
7. Simpson, J.; Woodley, W.L. Seeding Cumulus in Florida: New 1970 Results. *Science* **1971**, *172*, 117–126. [[CrossRef](#)]
8. Bennetts, D.A.; Bader, M.J.; Marles, R.H. Convective cloud merging and its effect on rainfall. *Nat. Cell Biol.* **1982**, *300*, 42–45. [[CrossRef](#)]

9. Simpson, J. Downdrafts as Linkages in Dynamic Cumulus Seeding Effects. *J. Appl. Meteorol.* **1980**, *19*, 477–487. [[CrossRef](#)]
10. Mladjen, C.; Dejan, J.; Vladan, V. The influence of merging and individual storm splitting on mesoscale convective system formation. *Atmos. Res.* **2009**, *93*, 21–29.
11. Tian, S.C. Effect of merging of the convective cloud clusters on occurrence of heavy rainfall. *Adv. Atmos. Sci.* **1991**, *8*, 499–504.
12. Bech, J.; Pineda, N.; Rigo, T.; Aran, M.; Amaro, J.; Gayà, M.; Arús, J.; Montanyà, J.; van der Velde, O. A Mediterranean nocturnal heavy rainfall and tornadic event. Part I: Overview, damage survey and radar analysis. *Atmos. Res.* **2011**, *100*, 621–637. [[CrossRef](#)]
13. Westcott, N.E.; Kennedy, P.C. Cell Development and Merger in an Illinois Thunderstorm Observed by Doppler Radar. *J. Atmos. Sci.* **1989**, *46*, 117–131. [[CrossRef](#)]
14. Daniel, C.; Angelika, P. The occurrence of convective systems with a bow echo in warm season in Poland. *Atmos. Res.* **2017**, *193*, 26–35.
15. French, A.J.; Parker, M.D. Observations of Mergers between Squall Lines and Isolated Supercell Thunderstorms. *Weather Forecast.* **2012**, *27*, 255–278. [[CrossRef](#)]
16. Zhou, A.; Zhao, K.; Lee, W.-C.; Huang, H.; Hu, D.; Fu, P. VDRAS and polarimetric radar investigation of a bow echo formation after a squall line merged with a preline convective cell. *J. Geophys. Res. Atmos.* **2020**, *125*, e2019JD031719. [[CrossRef](#)]
17. French, A.J.; Parker, M.D. Numerical Simulations of Bow Echo Formation Following a Squall Line–Supercell Merger. *Mon. Weather Rev.* **2014**, *142*, 4791–4822. [[CrossRef](#)]
18. LaPenta, K.D.; Bosart, L.F.; Galarneau, T.J.; Dickinson, M.J. A Multiscale Examination of the 31 May 1998 Mechanicville, New York, Tornado. *Weather Forecast.* **2005**, *20*, 494–516. [[CrossRef](#)]
19. Fujita, T.T. Manual of downburst identification for project NIMROD. *Univ. Chic. SMRP Res. Pap.* **1978**, *156*, 104.
20. Atkins, N.T.; Laurent, M.S. Bow Echo Mesovortices. Part I: Processes That Influence Their Damaging Potential. *Mon. Weather Rev.* **2009**, *137*, 1497–1513. [[CrossRef](#)]
21. Atkins, N.T.; Laurent, M.S. Bow Echo Mesovortices. Part II: Their Genesis. *Mon. Weather Rev.* **2009**, *137*, 1514–1532. [[CrossRef](#)]
22. Trapp, R.J.; Weisman, M.L. Low-level mesovortices within squall lines and bow echoes. Part II: Their Genesis and Implications. *Mon. Weather Rev.* **2003**, *131*, 2804–2823. [[CrossRef](#)]
23. Wakimoto, R.M.; Murphey, H.V.; Nester, A.; Jorgensen, D.P.; Atkins, N.T. High Winds Generated by Bow Echoes. Part I: Overview of the Omaha Bow Echo 5 July 2003 Storm during BAMEX. *Mon. Weather Rev.* **2006**, *134*, 2793–2812. [[CrossRef](#)]
24. Wakimoto, R.M.; Murphey, H.V.; Davis, C.A.; Atkins, N.T. High Winds Generated by Bow Echoes. Part II: The Relationship between the Mesovortices and Damaging Straight-Line Winds. *Mon. Weather Rev.* **2006**, *134*, 2813–2829. [[CrossRef](#)]
25. Weisman, M.L.; Trapp, R.J. Low-level mesovortices within squall lines and bow echoes. Part I: Overview and Dependence on Environmental Shear. *Mon. Weather Rev.* **2003**, *131*, 2779–2803. [[CrossRef](#)]
26. Xu, X.; Xue, M.; Wang, Y. The Genesis of Mesovortices within a Real-Data Simulation of a Bow Echo System. *J. Atmos. Sci.* **2015**, *72*, 1963–1986. [[CrossRef](#)]
27. Weisman, M.L. The Genesis of Severe, Long-Lived Bow Echoes. *J. Atmos. Sci.* **1993**, *50*, 645–670. [[CrossRef](#)]
28. Grim, J.A.; Rauber, R.M.; McFarquhar, G.M.; Jewett, B.F.; Jorgensen, D.P. Development and Forcing of the Rear Inflow Jet in a Rapidly Developing and Decaying Squall Line during BAMEX. *Mon. Weather Rev.* **2009**, *137*, 1206–1229. [[CrossRef](#)]
29. Peng, X.; Zhang, R.; Wang, H. Kinematic features of a bow echo in southern China observed with Doppler radar. *Adv. Atmos. Sci.* **2013**, *30*, 1535–1548. [[CrossRef](#)]
30. Wolf, P.L.; Wolf, R.; Przybylinski, R.W.; Berg, P. Observations of a merging bowing segment and supercell. In *18th Conference on Severe Local Storms, San Francisco, CA, USA, 13–23 February 1996*; American Meteorological Society: Boston, MA, USA; pp. 740–745.
31. Wolf, P.L. WSR-88D radar depiction of supercell-bow echo interaction: Unexpected evolution of a large, tornadic, ‘com-ma-shaped’ supercell over Eastern Oklahoma. *Weather Forecast.* **1998**, *13*, 492–504. [[CrossRef](#)]
32. Przybylinski, R.W. The Bow Echo: Observations, Numerical Simulations, and Severe Weather Detection Methods. *Weather Forecast.* **1995**, *10*, 203–218. [[CrossRef](#)]
33. Spiridonov, V.; Ćurić, M. Examination of physical processes of convective cell evolved from a MCS—Using a different model initialization. *Asia-Pac. J. Atmos. Sci.* **2016**, *52*, 263–279. [[CrossRef](#)]
34. Jou, B.J.-D.; Kao, Y.-C.; Hsiu, R.-G.R.; Jung, C.-J.U.; Lee, J.R.; Kuo, H.C. Observational Characteristics and Forecast Challenge of Taipei Flash Flood Afternoon Thunderstorm: Case Study of 14 June 2015. *Atmos. Sci.* **2016**, *44*, 57–82.
35. del Moral, A.; Weckwerth, T.M.; Rigo, T.; Bell, M.M.; Llasat, M.C. C-Band Dual-Doppler Retrievals in Complex Terrain: Improving the Knowledge of Severe Storm Dynamics in Catalonia. *Remote Sens.* **2020**, *12*, 2930. [[CrossRef](#)]
36. Snyder, J.C. Observations and Simulations of Polarimetric, X-Band Radar Signatures in Supercells. Ph.D. Thesis, University of Oklahoma, Norman, OK, USA, 2013.
37. Snyder, J.C.; Ryzhkov, A.V.; Kumjian, M.R.; Khain, A.P.; Picca, J. A ZDR Column Detection Algorithm to Examine Convective Storm Updrafts. *Weather Forecast.* **2015**, *30*, 1819–1844. [[CrossRef](#)]
38. Bringi, V.N.; Burrows, D.A.; Menon, S.M. Multiparameter Radar and Aircraft Study of Raindrop Spectral Evolution in Warm-based Clouds. *J. Appl. Meteorol.* **1991**, *30*, 853–880. [[CrossRef](#)]
39. Bringi, V.N.; Liu, L.; Kennedy, P.C.; Chandrasekar, V.; Rutledge, S.A. Dual multiparameter radar observations of intense convective storms: The 24 June 1992 case study. *Theor. Appl. Clim.* **1996**, *59*, 3–31. [[CrossRef](#)]
40. Brandes, E.A.; Vivekanandan, J.; Tuttle, J.D.; Kessinger, C.J. A study of thunderstorm microphysics with multiparameter radar and aircraft observations. *Mon. Weather Rev.* **1995**, *123*, 3129–3143. [[CrossRef](#)]

41. Smith, P.L.; Musil, D.J.; Detwiler, A.G.; Ramachandran, R. Observations of mixed-phase precipitation within a CaPE thunderstorm. *J. Appl. Meteorol.* **1999**, *38*, 145–155. [[CrossRef](#)]
42. Loney, M.L.; Zrnich, D.S.; Straka, J.M.; Ryzhkov, A.V. Enhanced polarimetric radar signatures above the melting level in a supercell storm. *J. Appl. Meteorol.* **2002**, *41*, 1179–1194. [[CrossRef](#)]
43. Kennedy, P.C.; Rutledge, S.A.; Petersen, W.A.; Bringi, V.N. Polarimetric Radar Observations of Hail Formation. *J. Appl. Meteorol.* **2001**, *40*, 1347–1366. [[CrossRef](#)]
44. Kumjian, M.R.; Ganson, S.M.; Ryzhkov, A.V. Freezing of Raindrops in Deep Convective Updrafts: A Microphysical and Polarimetric Model. *J. Atmos. Sci.* **2012**, *69*, 3471–3490. [[CrossRef](#)]
45. Kumjian, M.R.; Khain, A.P.; Benmoshe, N.; Ilotoviz, E.; Ryzhkov, A.V.; Phillips, V. The Anatomy and Physics of ZDR Columns: Investigating a Polarimetric Radar Signature with a Spectral Bin Microphysical Model. *J. Appl. Meteorol. Clim.* **2014**, *53*, 1820–1843. [[CrossRef](#)]
46. Chisolm, A.J.; Renick, J.H. *The Kinematics of Multicell and Supercell Alberta Hailstorms, Alberta Hail Studies, 1972, Research Council of Alberta Hail Studies Rep. No. 72-2*; Research Council of Alberta: Calgary, AB, Canada, 1972.
47. Kevin, R.K.; James, R.S.; Eugene, W.M. An observational and numerical study of a mini-supercell storm. *Atmos. Res.* **1998**, *49*, 35–63.
48. Sun, J.; Crook, N.A. Real-Time Low-Level Wind and Temperature Analysis Using Single WSR-88D Data. *Weather Forecast.* **2001**, *16*, 117–132. [[CrossRef](#)]
49. Ray, P.S.; Ziegler, C.L.; Bumgarner, W.; Serafin, R.J. Single- and Multiple-Doppler Radar Observations of Tornadic Storms. *Mon. Weather Rev.* **1980**, *108*, 1607–1625. [[CrossRef](#)]
50. Luo, C.G.; Chi, Y.Z.; Zhou, H.G. Characteristics of 3-D wind structure of typhoon outer intensive banded echo using dual-Doppler weather radar data. *Chin. J. Atmos. Sci.* **2012**, *36*, 247–258. (In Chinese)
51. Ouyang, S.C.; Chen, G.Y.; Lin, Y. *Information Digitization and Prediction*; China Meteorological Press: Beijing, China, 2009; pp. 154–196. (In Chinese)
52. Xu, C.Y.; Lin, Y.H.; Guan, Z.Y. The boundary layer characteristics of two types of mesoscale convective systems along a Meiyu front. *Trans. Atmos. Sci.* **2012**, *35*, 51–63.
53. Doviak, R.J.; Ray, P.S.; Strauch, R.G.; Miller, L.J. Error Estimation in Wind Fields Derived from Dual-Doppler Radar Measurement. *J. Appl. Meteorol.* **1976**, *15*, 868–878. [[CrossRef](#)]
54. Kong, F.Y.; Mao, J.T. A model study of three-dimensional wind field analysis from dual-Doppler radar data. *Adv. Atmos. Sci.* **1994**, *11*, 162–174.